Research Article

Ibrahim Mahariq, Umar Nazir, and Umair Khan*

# Computational works of blood flow with dust particles and partially ionized containing tiny particles on a moving wedge: Applications of nanotechnology

https://doi.org/10.1515/ntrev-2025-0150
received August 11, 2024; accepted August 7, 2025

**Abstract:** The effect of Hall and ion slip forces on a three-dimensional wedge flow with multiple slip conditions and hyperbolic tangent rheology is examined in the current problem. The flow and thermal behaviors are analyzed considering a ternary hybrid nanofluid (HNF) with a two-phase boundary layer mechanism with both liquid and dusty phases. Thermal energy characteristics involving nanofluid suspensions of copper, $TiO_2$, and aluminum oxide in an ethylene glycol utilizing the correlations of Yamada-Ota and Xue models. Viscous dissipation and Joule heating effects are also taken into account in the model, which is important for applications in a variety of industries, including papermaking, cooling systems, heat reservoirs and automotive thermal control. The governing PDEs are reduced to ODEs through the use of mathematical transformations. The numerical results are simulated by utilizing the finite element method. The findings show that, in comparison to the phase liquid, the dusty fluid moves more readily and has a thicker momentum boundary layer than the phase liquid. By highlighting the unique thermal and flow characteristics of each phase, these results advance our knowledge of the dynamics of HNFs. The new understanding of multi-phase, ternary HNFs under electromagnetic forces provided by this study improves the predictive modeling of nanofluid behaviors for industrial and engineering applications, particularly those that call for exact control and high thermal efficiency.

**Keywords:** dusty fluid, tangent hyperbolic martial, magnetoelectric slip influences, Joule heating, viscous dissipation

*** Corresponding author: Umair Khan**, Department of Mathematics, Saveetha School of Engineering, Saveetha Institute of Medical and Technical Sciences, Saveetha University, Chennai, 602105, Tamil Nadu, India; Department of Mathematics, Faculty of Science, Sakarya University, Serdivan/Sakarya, 54050, Turkey,
e-mail: umairkhan@sakarya.edu.tr
**Ibrahim Mahariq:** College of Engineering and Architecture, Gulf University for Science and Technology, Mishref, Kuwait; Najjad Zeenni Faculty of Engineering, Al Quds University, Jerusalem, Palestine; Applied Science Research Center, Applied Science Private University, Amman, Jordan; Department of Medical Research, China Medical University Hospital, China Medical University, Taichung, Taiwan; University College, Korea University, Seoul, Republic of Korea
**Umar Nazir:** Department of Mathematics, Faculty of Science, Khon Kaen University, Khon Kaen, 40002, Thailand

## Nomenclature

| | |
|---|---|
| $Al_2O_3$ | aluminum oxide |
| Cu | copper |
| $Cfx$, $Cfy$ | skin friction coefficients |
| $c_p$ | specific heat capacitance |
| Ec | Eckert number |
| $e$ | elements |
| FEM | finite element method |
| $k^*$ | volume fraction |
| $\mathcal{K}$ | thermal conductivity |
| $l_2$, $l_1$ | multiple slip coefficient numbers |
| $M$ | magnetic number |
| $m$ | power law index number |
| $N$ | drag force |
| Nu | Nusselt number |
| $n$ | stretching parameter |
| Pr | Prandtl number |
| $Q$ | heat source number |
| $\mathscr{Q}$ | dimensionless temperature |
| Re | Reynolds number |
| $T_p$ | temperature of dusty model |
| $T_\infty$ | ambient temperature |
| $T_w$ | wall temperature |
| $TiO_2$ | titanium dioxide |
| $\mathfrak{u}$, $\mathfrak{v}$, $\mathfrak{w}$ | velocity components |
| $\mathfrak{u}_p$, $\mathfrak{v}_p$, $\mathfrak{w}_p$ | velocity components of the dusty model |

| | |
|---|---|
| $\nu$ | kinematic viscosity |
| We | Weissenberg number |
| $y, z, x$ | space coordinates |
| $\gamma_1$ | fluid particle interaction |
| $\beta et_i$ | ion slip number |
| $\rho$ | density |
| $\rho p$ | density of dusty flow model |
| $s_3, s_1, s_2$ | volume fractions |
| $\delta_v$ | fluid particle interaction number |
| $\mu$ | kinematic viscosity |
| $\lambda_1, \lambda_2$ | multiple slip coefficients |
| $\infty$ | infinity |
| $\Gamma^e$ | time relaxation number |
| $\sigma$ | electrical thermal conductivity |
| $\beta et_e$ | Hall number |
| $\eta$ | independent variable |
| $\delta_1$ | slip parameters |
| $\Theta_p$ | dimensionless temperature of the dusty model |
| $\beta$ | pressure gradient number |

# 1 Introduction

Because of its uses in information technology, especially in contemporary devices, as well as its use as coolants in refrigeration and other engineering processes, nanofluids are becoming more and more important. In 1995, Choi and Eastman [1] introduced nanofluid. Shamshuddin *et al.* [2] experienced the part of nanofluid in the heat transfer mechanism using the impacts of solar radiation and Lorentz force. They visualized viscous dissipation and heat sinks on a stretching plate. Numerical outcomes are obtained using the shooting approach. The problem included that temperature profiles are improved when radiation, thermal viscosity, and heat source are increased because this increases the thermal conductivity of nanoparticles. Shamshuddin *et al.* [3] explored the features of heat transfer by highlighting the significance of Ohmic heating in nanofluid flow over a rotating disk and using ferromagnetic nanoparticles. Heat transfer rates are enhanced by higher thermal radiation and markedly slowed down by an increase in the Eckert number. Shamshuddin *et al.* [4] analyzed thermal characteristics utilizing water-based hybrid nanofluid (HNF) across a plate in the presence of convective conditions. The homotopy analysis method (HAM) approach is utilized for numerical purposes. Shamshuddin *et al.* [5] discussed the visualization of HNF in hyperbolic tangent rheology *via* a magnetic field on a rotating disk. They have utilized a semi-analytical scheme for numerical consequences. An HNF transfers heat more effectively than a mono nanofluid (NF), and our findings are in good agreement with other studies that have been published. Shamshuddin *et al.* [5] studied the influence of the Lorentz force involving NF with an Ohmic heating approach. They assumed base fluid ethylene glycol (EG) with the suspension of copper and silver. Nanoparticle concentrations decrease as reactive species and Lewis number increase, while the Sherwood number increases as a result of increased chemical reaction impact. Shamshuddin *et al.* [6] visualized thermal aspects in Prandtl liquid on a 3D plate with an Ohmic heating approach. They incorporated HNF along with base fluid (water) *via* slip solution (multiple). Numerical outcomes have been attained by the HAM approach. Kumar *et al.* [7] captured the influence of the Buongiorno model incorporating nanomaterials named aluminum oxide and Cu on the wedge. They used magnetic fields and two kinds of heat sources named linear and space-dependent heat sources. The Nusselt number for shaped nanoparticles is higher than that for spherical nanoparticles. Karthik *et al.* [8] visualized thermal analysis based on thermal radiation with tri-hybrid nanoparticles and thermo-phoretic particles toward a wedge. The numerical outcome is obtained using the shooting approach while the Sherwood number is declined when volume fraction and thermo-phoretic particles are increased. Sajid *et al.* [9] discussed autocatalysis reactions of cross NF across a wedge while heat energy characterizations were determined using thermal radiation and thermal conductivity (variable). They also utilized homogeneous heat sources and heterogeneous reactions on a wedge. Patil *et al.* [10] estimated the two-dimensional (2D) motion of micropolar fluid with viscous dissipation on a wedge utilizing the quasi-linearization approach. They utilized nanofluid for characterizations of thermal energy and microorganisms. Abbasi *et al.* [11] optimized the 2D motion of hybrid nanoparticles in a channel filled with hybrid nanoparticles. They utilized the Joule heating mechanism and solar radiation in the desired model. They determined entropy production in the presence of nanoparticles. Thermal energy declined when the magnetic number and suction number were increased. Saleem *et al.* [12] optimized the 2D motion of a magnetic field and hybrid nanomaterials on a plate utilizing mixed conditions and viscous dissipation. Flow behavior is analyzed using Newtonian fluid. They have used the Keller box approach for numerical purposes. Sagheer *et al.* [13] developed a model of Maxwell fluid including hybrid nanoparticles with assumptions of magnetic field and engine oil. They incorporated viscous dissipation and source (heat) where cases shooting scheme was utilized for numerical outcomes.

Sultana *et al.* [14] modified the model of a power-law fluid in the presence of ions slip and Hall forces on 2D surface and Joulean dissipation. They inserted an HNF with convective conditions. RK-4 numerical approach is

employed for numerical outcomes. They included that flow behavior for ion slip and Hall force becomes significant. Gul *et al.* [15] estimated the performance of tri-hybrid nanoparticles including reactions (heterogeneous and homogeneous) numerically simulated by the bvp4c approach. They used the non-Fourier's method in the heat transfer equation. Thermal efficiency for tri-hybrid nanofluids (THNFs) is higher than thermal efficiency for hybrid nanofluids (HBNfs). Das *et al.* [16] developed a model related to partial ionization with the occurrence of peristaltic liquid on a microchannel. They estimated that motion (nanoparticles) declined when the ion slip number was enhanced. Krishna and Chamkha [17] observed the motion of hybrid nanoparticles with the appearance of solar radiation and slip conditions on surfaces subjected to partial ionization. The velocity field is inclined when the slip number, Hall number, and buoyancy parameter are enhanced. Kodi *et al.* [18] presented the impacts of Joule heating in the motion (hybrid nanoparticles) with Hall currents on the surface. They assumed thermophoresis, chemical reaction, no-slip conditions and Brownian parameters. Numerical outcomes are obtained using a shooting scheme. Jameel *et al.* [19] discussed the role of 3D flow and HNF and entropy production on 3D surfaces (stretching and shrinking). They assumed non-Fourier's method for knowing heat energy and partial ionizations. Sharif *et al.* [20] utilized a Riga plate and took the volume concentration of the dust material while the study investigated the momentum and thermal properties of magnetohydrodynamics (MHD)-Ellis ternary nanomaterial integrated with dust particles. Khan *et al.* [21] explored dusty tetra HNF that effortlessly meanders between infinite vertical parallel stationary panels through convection. Furthermore, the entire stream is evenly scattered with spherical dust particles. Using non-Fourier mechanisms and MHD boundary layers on various shapes, including plates, cones, and wedges, Babu *et al.* [22] examined heat energy estimation. Using the RK-4 method, they examined the behavior of Brownian and thermophoresis particles and calculated skin friction coefficients under various parameter variations. The idea of variable thermal properties and a mixed convective approach incorporating hydro-magnetic mechanisms were investigated by Awais *et al.* [23]. Using the optimal homotopy asymptotic method approach, they looked into the absorption and generation of non-Newtonian liquids based on heat sources. Akbar *et al.* [24] estimated the thermal enhancement incorporating heat sink effects in a non-Newtonian (Jeffrey) model filled with hybrid nanofluids. They studied the impact of peristaltic motion including entropy generation. They have used a finite element approach. Akbar *et al.* [25] discussed the impact of energy transfer with the suspension of multiple NFs in symmetric ducts with pores considering the phenomena of peristaltic motion. They discussed the role of carbon nanotubes (CNTs). Adhikari *et al.* [26] observed the influence of tetra-HNF in Maxwell–Oldroyd-B liquid considering blood motion in an elastic artery utilizing Neural networks. They have included that the opposite trend has been noticed in thermal energy and velocity field when the Lorentz force has been used. Paul *et al.* [27] explored the impact of ion slip and Hall current with titania-CNTs in a base fluid (blood) under the role of electro-magnetization in a squeezed artery. It was estimated that drag force has been enhanced utilizing a higher Hall number and ion slip number. Lund *et al.* [28] determined the role of sodium alginate with an HNF on a moving surface under the effect of Joule heating and radiation toward a stretching plate. Lund *et al.* [29] observed the dual solutions of steady motion in Casson flow on a shrinking sheet incorporating the Lorentz force. They implemented a stability approach. The works associated with heat transfer with nanofluid are discussed in previous literature [30–39]. Figure 1a describes the applications of HNF. The applications of HNF include automotive cooling process, solar energy, biomedical field, material characteristic, lubrication, welding process, air conditioning and cooling coils.

Table 1 shows the uniqueness of the current model. The research questions related to the current study are listed as follows:

- What will be the variation in velocity curves on enhancing values of Hall number, $\beta$, and ion slip number?
- How will the effect of divergent velocity on Hall number, magnetic number, and ion slip number be?
- What will be the comparative effects between working fluid, nano, hybrid, and tri-HNF on heat energy?
- How do magnetic, Hall, ion slip, and magnetic parameters influence on temperature profile?
- What will be the comparative roles of dusty and phase fluid on temperature and velocity curves?

Table 1 describes the novelty study of the developed model. The influences in the current model have not yet *via* published works [40–43]. The effects based on tri-HNF, dusty fluid, Hall and ion slip impacts on 3D wedge are not discussed in the current model utilizing FEM. Hence, the current model shows strong novelty work.

The current model has some limitations which are listed below.

- Certain terms add complexity, such as those about the magnetic field $M$, slip parameters $\delta_1$, and ion slip terms $\beta$. Interpreting the sensitivity of each of these parameters is crucial for validation because even slight changes could have a big impact on the results;

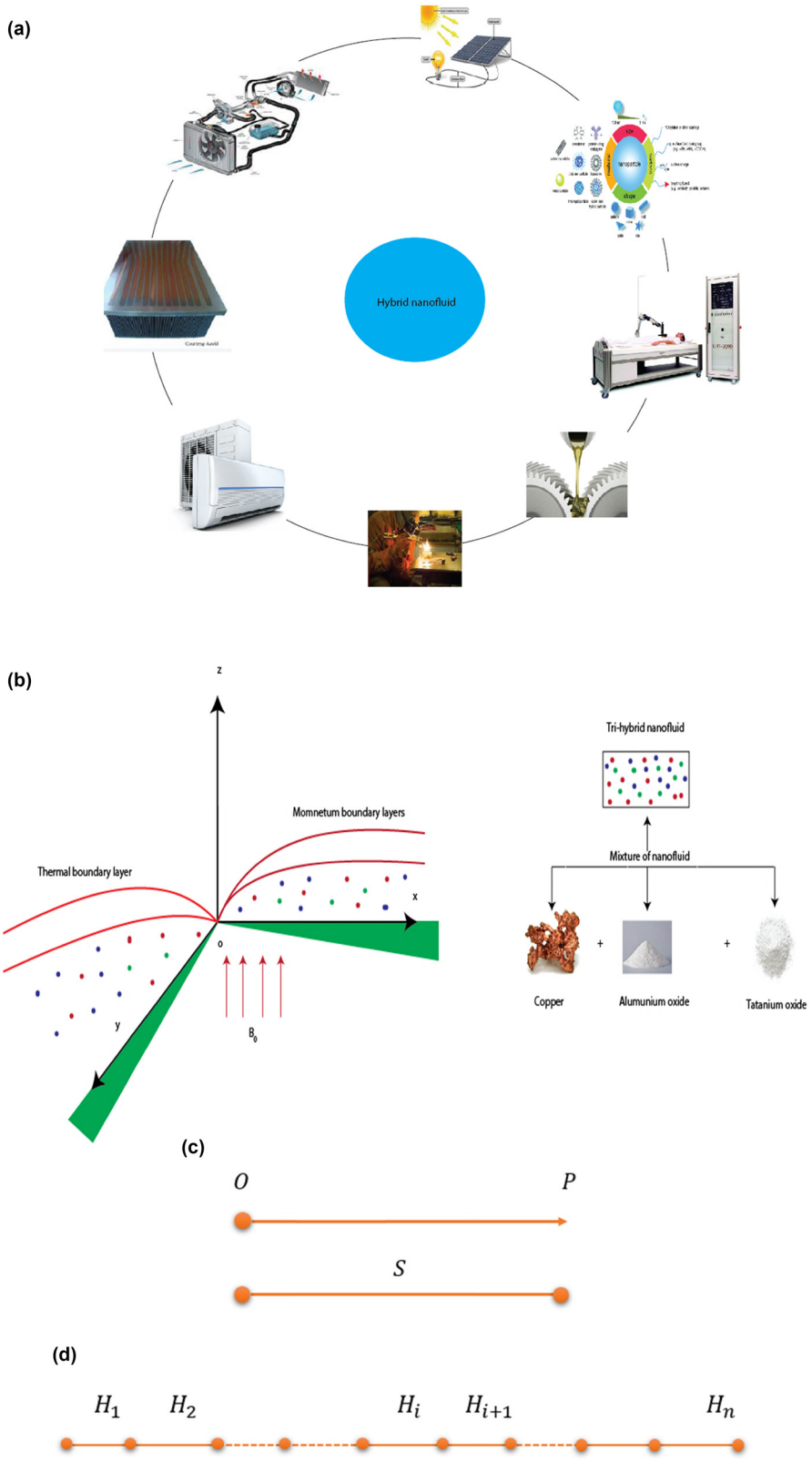


**Figure 1:** (a) Applications of HNF. (b) Flow chart of desired model and mixture of NF. (c) Conversion of c-domain. (d) Elements with subdomain.

**Table 1:** Novelty study of the present developed model

| Authors | Hall and ion slip forces | Dusty fluid | Tri-HNF | 3D wedge | Hyperbolic tangent fluid | Finite element method (FEM) |
|---|---|---|---|---|---|---|
| Rana *et al.* [40] | × | × | × | ✓ | × | × |
| Kudenatti *et al.* [41] | × | × | × | ✓ | × | × |
| Kudenatti and Jyothi [42] | × | × | × | ✓ | × | × |
| Rana and Gupta [43] | × | × | × | ✓ | × | × |

- Convergence issues may arise from nonlinear terms in the equations, such as those involving $F'''$, $g'''$, and products of derivatives;
- FEM uses interpolation within each element to approximate solutions, which can result in discretization errors, particularly in regions with steep gradients. In models with intricate interactions, like ternary HNFs, these errors may compound for high-order derivatives, potentially decreasing accuracy.

Current work investigates the effects of ion and Hall slip forces on 3D wedge with particular attention to thermal and flow behaviors in a ternary HNF considering liquid and dusty phases. The FEM to model the behavior of NF suspensions (copper, $TiO_2$, and $Al_2O_3$) under Joule heating and viscous dissipation.

## 2 Mathematical background of the flow problem

Let us consider a steady, laminar, and three-dimensional incompressible boundary layer flow of tangent hyperbolic and dusty particles towards a wedge shape object with slip boundary conditions. According to geometry, flow is considered at $z > 0$ and $z$-coordinates are assumed upright on the $yx$-plane. Hall currents along with ion slip forces are assumed in energy as well as momentum equations. Viscous dissipation is assumed along with the Joule heating mechanism in the energy equation. The relations of three types (NF) called ternary HNF are incorporated. The HNF model is known as Y Ota and Xue-models are taken out. Dusty model is assumed with suspension of ternary HNF. Thermal properties associated with various nanofluids are assumed in Table 2. A diagram of the 3D wedge is assumed in Figure 1b.

**Table 2:** Thermal properties are associated with nanoparticles [45]

| Properties | Aluminum oxide | Copper | $TiO_2$ | Ethylene glycol |
|---|---|---|---|---|
| $k$ | 40 | 401 | 8.9538 | 0.253 |
| $\rho$ | 3,970 | 8,933 | 4,250 | 1113.5 |
| $C_p$ | 765 | 385 | 686.2 | 2,430 |

Figure 1b describes a 3D wedge surface in $z, x$, and $y$ components. In Figure 1b, the green shaded region reveals a wedge expanding in $y$ and $x$ coordinates. The $x$-axis is the orientation of the wedge, and fluid flow passes over this geometry. It is mentioned that the horizontal direction is visualized by the $x$-axis, the $y$-axis is placed along the perpendicular direction, and the $z$-axis shows vertically upwards. An applied magnetic field that is perpendicular to the wedge surface is indicated by red arrows pointing upward. Momentum and thermal boundary layers are indicated by two lines. A tri-HNF is created by combining three different types of nanoparticles: copper, aluminum oxide, and titanium oxide. $T_w$ and $T_\infty$ are called wall temperature and ambient temperature placed at the wall and for a way of the wall. The wall velocities along $y$- and $x$-directions are assumed as $\mathfrak{u}_w$ and $\mathfrak{v}_w$. The assumptions are listed below.

- Three-dimensional motion of hyperbolic tangent liquid is considered;
- Steady flow and incompressible flow are assumed;
- Dusty flow model is assumed;
- Viscous dissipation and Joule heating are considered;
- The heat sink is utilized;
- Multiple conditions are incorporated;
- The suspension of tri-HNF is inserted;
- The 3D-wedge surface is considered.

Reduced ordinary differential equations (ODES) using boundary layer approximations (in conservation laws) [40] are derived as

$$\mathfrak{u}_x + \mathfrak{v}_y + \mathfrak{w}_z = 0, \tag{1}$$

$$\begin{aligned} &\mathfrak{u}\mathfrak{u}_x + \mathfrak{v}\mathfrak{u}_y + \mathfrak{w}\mathfrak{u}_z \\ &= \mathfrak{u}\mathfrak{u}_x + \mathfrak{v}\mathfrak{v}_x + \nu_{\text{thnf}}[(1-n)\mathfrak{u}_{zz} + \sqrt{2}n\Gamma^e\mathfrak{u}_z\mathfrak{u}_{zz}] \\ &\quad + \frac{k^*N}{\rho_{\text{thnf}}}(\mathfrak{v}_y - \mathfrak{v}) + \frac{\sigma_{\text{thnf}(B_0)^2}}{\rho_{\text{thnf}}[(1+\beta et_e\beta et_i)^2 + (\beta et_e)^2]} \\ &\quad \times (\mathfrak{v}\beta et_e - (1+\beta et_i\beta et_e)\mathfrak{u}), \end{aligned} \tag{2}$$

$$\begin{aligned}\mathbb{u}\mathbb{v}_x + \mathbb{v}\mathbb{v}_y + \mathbb{w}\mathbb{v}_z &= \mathbb{u}\mathbb{v}_x + \mathbb{v}\mathbb{v}_y + \nu_{\text{thnf}}[(1-n)\mathbb{v}_{zz} \\ &+ \sqrt{2}n\Gamma^e\mathbb{v}_z\mathbb{v}_{zz}] + \frac{k^*N}{\rho_{\text{thnf}}}(\mathbb{u}_p \ \ \mathbb{u}) \\ &- \frac{\sigma_{\text{thnf}(B_0)^2}}{\rho_{\text{thnf}}[(1+\beta et_e\beta et_i)^2 + (\beta et_e)^2]} \\ &\times (\mathbb{u}\beta et_e + (1+\beta et_i\beta et_e)\mathbb{v}),\end{aligned} \tag{3}$$

$$\begin{aligned}\mathbb{u}T_x + \mathbb{v}T_y + \mathbb{w}T_z &= \frac{\mathcal{K}_{\text{thnf}}}{(\rho c_{\text{p}})_{\text{thnf}}}T_{zz} \\ &+ \frac{\sigma_{\text{thnf}(B_0)^2}}{\rho_{\text{thnf}}[(1+\beta et_e\beta et_i)^2 + (\beta et_e)^2]} \\ &\times (\mathbb{u}^2 + \mathbb{v}^2) + \frac{\mu_{\text{thnf}}}{(\rho c_{\text{p}})_{\text{thnf}}}\Bigg[\Bigg(1-n \\ &+ \frac{n\Gamma^e}{(2)^{\frac{1}{2}}}((\mathbb{u}_z)^2 + (\mathbb{v}_z)^2)^{\frac{1}{2}}\Bigg) \\ &\times \Bigg(((\mathbb{u}_z)^2 + (\mathbb{v}_z)^2)^{\frac{1}{2}}(\mathbb{u}_z^2 + \mathbb{v}_z{}^2)\Bigg] \\ &+ \frac{Q}{(\rho c_{\text{p}})_{\text{thnf}}}(T - T_\infty) \\ &+ \frac{NC_{pf}m}{\rho c_p\tau_t}(T_p - T).\end{aligned} \tag{4}$$

Slip conditions (multiple) are considered [40] as

$$\begin{aligned}&\mathbb{u} = \mathbb{u}_w + l_1\mathbb{u}_z, \mathbb{v} = \mathbb{v}_w + l_2\mathbb{v}_z, \mathbb{w} = 0, \quad T = T_w : z = 0, \\ &\mathbb{u} \to \mathbb{U}, \mathbb{v} \to \mathbb{V}, T \to T_\infty : z \to \infty, \mathbb{u}_p \to 0, \\ &\mathbb{v}_p \to 0, \quad \mathbb{w}_p \to 0, \quad T_p \to \infty,\end{aligned} \tag{5}$$

Boundary conditions (BCs) at $z = 0$, velocity along the $x$-direction is $\mathbb{u}_w + l_1\mathbb{u}_z$, here $\mathbb{u}_w$ is the wall velocity while it is generated using slip condition. $l_1\mathbb{u}_z$ is called velocity gradient, which is generated at no-slip condition. $l_1$ reveals the varying linear velocity. Velocity along the $x$-direction is $\mathbb{v}_w + l_2\mathbb{v}_z$. $\mathbb{v}_w$ is the wall velocity along the y-component. $l_2\mathbb{v}_z$ describes a linear velocity gradient that describes possible slip or no slip based on $l_2$. $\mathbb{w}$ shows velocity direction along the $z$-direction. At $\mathbb{w} = 0$, it means that flow is not occurred. $T = T_w$ means that the temperature of the fluid at the wall is the same as that of the wall. BCs at $z \to \infty$, $\mathbb{u} \to \mathbb{U}$, and $\mathbb{v} \to \mathbb{V}$ reveal that at large distances from the wall, the fluid flow becomes uniform. $T \to T_\infty$ reveals that the fluid's temperature is approached to $T_\infty$. $\mathbb{u}_p$, $\mathbb{v}_p$, and $\mathbb{w}_p$ are velocity components for the dusty fluidic model. $\mathbb{u}_p \to 0$, $\mathbb{v}_p \to 0$, and $\mathbb{w}_p \to 0$ means that fluid flow becomes uniform and steady. $T_p \to \infty$ means that temperature decreases far from the wall as a result of wall effects. Transformations for phase fluid and dusty fluid are defined [40] as

$$\begin{aligned}\mathbb{u} &= \mathbb{U}_\infty(x+y)^n\mathcal{F}', \\ \mathbb{v} &= \mathbb{v}_\infty(x+y)^n g', \\ \eta &= z\left(\frac{\mathbb{U}(1+n)\nu_f}{(x+y)2\nu_f}\right)^{1/2}, \\ T &= Q(T_w - T_\infty) + T_\infty, \\ \mathbb{w} &= -\left(\frac{\mathbb{U}_\infty(1+n)\nu_f}{2}\right)^{\frac{1}{2}}(x+y)^{\frac{n-1}{2}} \\ &\times \left[\mathcal{F} + \gamma g + \frac{n-1}{n+1}\eta(\mathcal{F}' + \gamma g')\right], \\ T_p &= (T_w - T_\infty)\Theta_p + T_\infty, \\ \mathbb{u}_p &= \mathbb{U}_\infty(x+y)^n\mathcal{F}_p', \quad \mathbb{v}_p = \mathbb{v}_\infty(x+y)^n g_p', \\ \mathbb{w}_p &= -\left(\frac{\mathbb{U}_\infty(1+n)\nu_f}{2}\right)^{\frac{1}{2}}(x+y)^{\frac{n-1}{2}}(\mathcal{F}_p + g_p).\end{aligned} \tag{6}$$

On incorporating transformations in governing the above equations, the ODEs [40] become

$$\begin{aligned}&(1-m)\mathcal{F}''' + m\text{We}\mathcal{F}''\mathcal{F}''' - \mathcal{F}''(\mathcal{F} + \gamma g) + \beta(1 - \mathcal{F}'^2) \\ &+ \gamma\beta(1 - \mathcal{F}'g') + \delta_1\gamma_1(\mathcal{F}_p' + \mathcal{F}') \\ &+ \frac{M^2}{(1+\beta et_e\beta et_i)^2 + (\beta et_e)^2}(\beta et_e g \\ &\times (1+\beta et_e\beta et_i)\mathcal{F}') = 0,\end{aligned} \tag{7}$$

$$\begin{aligned}&(1-m)g''' + m\text{We}g''g''' - g''(\mathcal{F} + \gamma g) + \beta(1 - g\mathcal{F}) \\ &+ \gamma\beta(1 - (g')^2) + \delta_1\gamma_1(g_p' + g') \\ &- \frac{M^2}{(1+\beta et_e\beta et_i)^2 + (\beta et_e)^2}(\beta et_e\mathcal{F}' \\ &+ (1+\beta et_e\beta et_i)g') = 0,\end{aligned} \tag{8}$$

$$\begin{aligned}&Q'' + Q'(\mathcal{F} + \gamma g) + \frac{k_{\text{f}}}{k_{\text{thnf}}}\frac{M^2\text{EcPr}}{(1+\beta et_e\beta et_i)^2 + (\beta et_e)^2}(\mathcal{F}'^2 \\ &+ g'^2) + \frac{k_{\text{f}}}{2k_{\text{thnf}}}\frac{\text{WePrEc}}{(1-s_3)^{2.5}(1-s_2)^{2.5}(1-s_1)^{2.5}} \\ &\times (\mathcal{F}''^2 + g''^2)^{1/2}(\mathcal{F}''^2 + g''^2) - \gamma_*\beta_*\text{Pr}(\Theta_p' \ \ Q) \\ &+ \frac{k_{\text{f}}}{k_{\text{thnf}}}\frac{\text{EcPr}}{(1+\beta et_e\beta et_i)^2 + (\beta et_e)^2}(\mathcal{F}''^2 + g''^2) = 0.\end{aligned} \tag{9}$$

Model associated with ternary HNF [44] is delivered as

$$\frac{\mu_{\text{f}}}{(1-s_3)^{2.5}(1-s_2)^{2.5}(1-s_1)^{2.5}} = \mu_{\text{thb}}, \tag{10}$$

$$\begin{aligned}\rho_{\text{thb}} &= (1-s_1)\{(1-s_2)[(1-s_3)\rho_{\text{f}} + s_3\rho_3] + s_2\rho_2\} \\ &+ s_1\rho_1,\end{aligned} \tag{11}$$

$$\frac{K_{\mathrm{hb}}}{K_{\mathrm{nf}}} = \frac{K_2 + 2K_{\mathrm{nf}} - 2s_1(K_{\mathrm{nf}} - K_2)}{K_2 + 2K_{nf} + s_2(K_{\mathrm{nf}} - K_2)}, \quad \frac{K_{\mathrm{thb}}}{K_{\mathrm{hb}}} = \frac{K_1 + 2K_{\mathrm{hb}} - 2s_1(K_{\mathrm{hb}} - K_1)}{K_1 + 2K_{\mathrm{hb}} + s_1(K_{\mathrm{hb}} - K_1)}, \tag{12}$$

$$\frac{K_{\mathrm{nf}}}{K_{\mathrm{f}}} = \frac{K_3 + 2K_{\mathrm{f}} - 2s_3(K_f - K_3)}{K_3 + 2K_{\mathrm{f}} + s_3(K_f - K_3)}, \quad \frac{\sigma_{\mathrm{nf}}}{\sigma_{\mathrm{f}}} = \frac{\sigma_3(1 + 2s_3) + s_{\mathrm{f}}(1 - 2s_3)}{\sigma_3(1 - s_3) + \sigma_{\mathrm{f}}(1 + s_3)}, \tag{13}$$

$$\frac{\sigma_{\mathrm{thb}}}{\sigma_{\mathrm{hb}}} = \frac{\sigma_1(1 + 2s_1) - \mathcal{F}_{\mathrm{hb}}(1 - 2s_1)}{\sigma_1(1 - s_1) + \sigma_{\mathrm{hb}}(1 + s_1)}, \quad \frac{\sigma_{\mathrm{hb}}}{\sigma_{\mathrm{nf}}} = \frac{\sigma_2(1 + 2s_2) + \varphi_{\mathrm{nf}}(1 - 2s_2)}{\sigma_2(1 - s_2) + \sigma_{\mathrm{nf}}(1 + s_2)}. \tag{14}$$

The Xue model (ternary hybrid) [44] is defined as

$$\frac{K_{\mathrm{Thb}}}{K_{\mathrm{nf}}} = \frac{1 - s_3 + 2s_3\left(\frac{K_1}{K_1 - K_{\mathrm{hb}}}\right)\ln\left(\frac{K_1 + K_{\mathrm{hb}}}{2K_{\mathrm{hb}}}\right)}{1 - s_3 + 2s_3\left(\frac{K_{\mathrm{hb}}}{K_1 - K_{\mathrm{hb}}}\right)\ln\left(\frac{K_1 + K_{\mathrm{hb}}}{2K_{\mathrm{hb}}}\right)}, \tag{15}$$

$$\frac{K_{\mathrm{hb}}}{K_{\mathrm{nf}}} = \frac{1 - s_3 + 2s_3\left(\frac{K_2}{K_2 - K_{\mathrm{nf}}}\right)\ln\left(\frac{K_2 + K_{\mathrm{nf}}}{2K_{\mathrm{hb}}}\right)}{1 - s_3 + 2s_3\left(\frac{K_{\mathrm{nf}}}{K_2 - K_{\mathrm{nf}}}\right)\ln\left(\frac{K_2 + K_{\mathrm{nf}}}{2K_{\mathrm{nf}}}\right)}, \tag{16}$$

$$\frac{K_{\mathrm{nf}}}{K_{\mathrm{f}}} = \frac{1 - s_1 + 2s_1\left(\frac{K_3}{K_3 - K_{\mathrm{f}}}\right)\ln\left(\frac{K_3 + K_{\mathrm{f}}}{2K_{\mathrm{f}}}\right)}{1 - s_3 + 2s_3\left(\frac{K_{\mathrm{f}}}{K_3 - K_{\mathrm{f}}}\right)\ln\left(\frac{K_3 + K_{\mathrm{f}}}{2K_{\mathrm{f}}}\right)}. \tag{17}$$

The Xue model (ternary hybrid) [44] is derived as

$$\frac{K_{\mathrm{hb}}}{K_{\mathrm{nf}}} = \frac{\left(\frac{K_{\mathrm{hb}}}{K_1}\right) + 2s_3^{0.2}\frac{L}{R} - 2s_3s_3^{0.2}\frac{L}{R}\left(1 - \frac{K_{\mathrm{hb}}}{K_1}\right)}{\left(\frac{K_{\mathrm{hb}}}{K_1}\right) + 2s_3^{0.2}\frac{L}{R} - s_3\left(1 - \frac{K_{\mathrm{hb}}}{K_1}\right)}, \tag{18}$$

$$\frac{K_{\mathrm{hb}}}{K_{\mathrm{nf}}} = \frac{\left(\frac{K_{\mathrm{nf}}}{K_2}\right) + 2s_2^{0.2}\frac{L}{R} - 2s_2s_2^{0.2}\frac{L}{R}\left(1 - \frac{K_{\mathrm{nf}}}{K_2}\right)}{\left(\frac{K_{\mathrm{nf}}}{K_2}\right) + 2s_2^{0.2}\frac{L}{R} - s_3\left(1 - \frac{K_{\mathrm{nf}}}{K_2}\right)}, \tag{19}$$

$$\frac{K_{\mathrm{nf}}}{K_{\mathrm{f}}} = \frac{\left(\frac{K_{\mathrm{f}}}{K_3}\right) + 2s_1^{0.2}\frac{L}{R} - 2s_1s_1^{0.2}\frac{L}{R}\left(1 - \frac{K_{\mathrm{f}}}{K_3}\right)}{\left(\frac{K_{\mathrm{f}}}{K_3}\right) + 2s_1^{0.2}\frac{L}{R} - s_1\left(1 - \frac{K_{\mathrm{f}}}{K_3}\right)}. \tag{20}$$

The model of dusty fluid [45] is mentioned below

$$(\mathrm{u}_p)_x + (\mathrm{v}_p)_y + (\mathrm{w}_p)_z = 0, \tag{21}$$

$$\mathrm{u}_p(\mathrm{u}_p)_x + \mathrm{v}_p(\mathrm{u}_p)_y + \mathrm{w}_p(\mathrm{u}_p)_z = \frac{Kn}{\rho p}(\mathrm{u} \quad \mathrm{u}_p), \tag{22}$$

$$\mathrm{u}_p(\mathrm{v}_p)_x + \mathrm{v}_p(\mathrm{v}_p)_y + \mathrm{w}_p(\mathrm{v}_p)_z = \frac{Kn}{\rho p}(\mathrm{v} \quad \mathrm{v}_p), \tag{23}$$

$$\mathrm{u}_p(T_p)_x + \mathrm{v}_p(T_p)_y + \mathrm{w}_p(T_p)_z = \frac{c_p}{c_m\tau_t}(T - T_p). \tag{24}$$

On utilizing transformations of the dusty model in PDEs of dusty model, the PDEs become

$$(\mathcal{F}_p + g_p)\mathcal{F}''_p - (\mathcal{F}'_p)^2 - g'_p\mathcal{F}'_p + \delta_v(\mathcal{F} \quad \mathcal{F}'_p) = 0, \tag{25}$$

$$(\mathcal{F}_p + g_p)g''_p - (g'_p)^2 - g'_p\mathcal{F}'_p + \delta_v(g \quad g'_p) = 0, \tag{26}$$

$$(\mathcal{F}_p + g_p)\Theta'_p + \lambda\delta_t(\Theta - \Theta_p) = 0. \tag{27}$$

BCs (dimensionless) are

$$\begin{aligned} &\mathcal{F} = 0, \quad g = 0, \quad \mathcal{F}' = \lambda_1 + \alpha_1\mathcal{F}'', \quad g' = \lambda_2 + \alpha_2 g'', \\ &\Theta = 1 + \alpha_3\Theta' : \eta = 0, \\ &\mathcal{F} \to 1, \quad g' \to 1, \Theta \to 0 : \eta \to \infty, \mathcal{F}'_p \to 0, \\ &g'_p \to 0, \quad \mathcal{F}_p \to \mathcal{F}, g_p \to g, \Theta_p \to 0. \end{aligned} \tag{28}$$

The shear stresses of walls [40] are reduced as

$$Cfx = \frac{\tau_{xz}}{(u_w)^2\rho_{\mathrm{thnf}}}, \quad (\mathrm{Re})^{-\frac{1}{2}}Cfx = \nu_{\mathrm{thnf}}\left[(1 - n)\mathcal{F}''(0) + \frac{n}{2}\mathrm{We}\mathcal{F}''(0)\right], \tag{29}$$

$$Cfy = \frac{\tau_{yz}}{(u_w)^2\rho_{\mathrm{thnf}}}, \quad (\mathrm{Re})^{-\frac{1}{2}}Cfy = \nu_{\mathrm{thnf}}\left[(1 - n)g''(0) + \frac{n}{2}\mathrm{We}g''(0)\right]. \tag{30}$$

Nusselt number [40] is

$$(\mathrm{Re})^{-\frac{1}{2}}\mathrm{Nu} = -\frac{K_{\mathrm{thnf}}}{k_{\mathrm{f}}}\Theta'(0). \tag{31}$$

# 3 Numerical approach

The ability of FEM to produce physically plausible solutions, which are distinguished by consistency, stability, and convergence, makes it a reliable numerical technique that is highly valued. Its adaptability makes it a popular option for mathematicians, physicists, and engineers because it can precisely handle complex geometries. Because of its versatility concerning different BCs and material properties, FEM [44] is frequently utilized in structural analysis and computational fluid dynamics.

The advantages of FEM are listed below.

- FEM handles irregular shapes and complex geometries;
- Fluid dynamics, heat transfer, electromagnetics, structural analysis, and many other fields can all benefit from the high versatility of FEM;
- Depending on the problem's complexity, FEM can frequently produce precise answers without requiring a large amount of processing power;
- Implementing different BCs, such as Robin, Neumann, and Dirichlet is a good fit for EM.
- FEM is beneficial for an extensive range of applications, from straightforward linear models to intricate three-dimensional structures, since it can solve problems in 1D, 2D, and 3D. It also addresses multiphysics problems, such as fluid-structure interaction, in which several physical phenomena interact at the same time.

A structured mesh is created by dividing the computational domain into smaller subdomains, $\mathrm{Dom}_i$, for $i = 1, 2, \ldots, m$. Each subdomain is connected at nodes ($i$th). Discrete analysis is based on the two nodes that make up each line segment. In Figure 1c, the semi-infinite domain is depicted, offering a structure for numerical calculations. This segmentation facilitates the effective application of BCs and partial differential equation solutions. Figure 1d illustrates the division of the subdomain.

The computational domain is described by $S$ = OP and $P$ is the point (where BCs are satisfied). The formulations are formulated on $S$. OP is divided into small elements $\mathrm{Dom}_i$.

$$\mathrm{Dom}_i = [\eta_i, \quad \eta_{i+1}, \eta_i]. \tag{32}$$

KL is defined as

$$\mathrm{KL} = 0, \xi \in D. \tag{33}$$

The discretization of problems with weights function is

$$\int K\left(\sum_{i=1}^{n} H_i \Psi_i\right) \Psi_j \mathrm{d}\Omega = 0. \tag{34}$$

The system of the equation is

$$AH_i = b, \tag{35}$$

where $A$ is a matrix (order $n \times n$) consisting of nodal values ($H_i$). A particular element is then used to integrate the weighted residuals.

$$L_h = \sum_{i=1}^{n} H_i \Psi_i, \tag{36}$$

where $H_i = F_i, G_i, K_i, Q_i$ The convergence criterion is

$$maX|\pi_i^{rr} - \pi_i^{rr-1}| < 10^{-5}. \tag{37}$$

### 3.1 Convergence analysis

The computed data from the grid independence study is displayed in Table 3. In Table 3, simulations of velocity and temperature fields are recorded when the number of elements is increased from 30 to 300. The data, which are taken at the halfway point of each element, demonstrate that the solution converges and remains unaffected by element additions. The current computational study is predicated on the conclusion that the solution stabilizes at 300 elements. Table 4 reveals the validation of the code with the polished study [40] for divergent velocities when $\beta et_i = \beta et_e = 0$ and We = 0.

## 4 Results and discussion

In Section 3, the complex system of ODEs related to phase fluid and dusty phase in the presence of correlations

**Table 3:** Mesh-free analysis of $\Theta_p\left(\frac{\eta_{\max}}{2}\right)$, $\mathscr{g}_p\left(\frac{\eta_{\max}}{2}\right)$, $\mathscr{F}_p\left(\frac{\eta_{\max}}{2}\right)$, $\mathscr{g}'\left(\frac{\eta_{\max}}{2}\right)$, and $\mathscr{F}'\left(\frac{\eta_{\max}}{2}\right)$

| $e$ | $\mathscr{F}'\left(\frac{\eta_{\max}}{2}\right)$ | $\mathscr{g}'\left(\frac{\eta_{\max}}{2}\right)$ | $\mathscr{Q}\left(\frac{\eta_{\max}}{2}\right)$ | $\mathscr{F}_p\left(\frac{\eta_{\max}}{2}\right)$ | $\mathscr{g}_p\left(\frac{\eta_{\max}}{2}\right)$ | $\Theta_p\left(\frac{\eta_{\max}}{2}\right)$ |
|---|---|---|---|---|---|---|
| 30 | 0.0234056466 | 0.0580435689 | 0.182239869 | 0.9890556832 | 0.2659396979 | 0.95097991372 |
| 60 | 0.09263981983 | 0.3326258029 | 0.178586925 | 0.8920320869 | 0.2309859091 | 0.75464761241 |
| 90 | 0.4161099304 | 0.5497993056 | 0.175164793 | 0.8089596326 | 0.1996852665 | 0.48848906700 |
| 120 | 0.4161099304 | 0.7030324797 | 0.171514050 | 0.7298820903 | 0.1716998880 | 0.38762269459 |
| 150 | 0.3662510383 | 0.8252500601 | 0.168707319 | 0.6554327134 | 0.1466935768 | 0.30411698221 |
| 180 | 0.5154292282 | 0.9969330760 | 0.166264252 | 0.5859876737 | 0.1043059661 | 0.23538172380 |
| 210 | 0.7460303502 | 0.0050345183 | 0.166044450 | 0.5217220983 | 0.08629197592 | 0.17292551291 |
| 240 | 0.0561544901 | 0.1427694011 | 0.165840482 | 0.4626561634 | 0.06999381097 | 0.09279069767 |
| 270 | 0.05623969901 | 0.14821369710 | 0.165423453 | 0.3596480640 | 0.05691248717 | 0.08886785565 |
| 300 | 0.05623100901 | 0.14825871639 | 0.165423775 | 0.3596760803 | 0.05695862297 | 0.08882114377 |

**Table 4:** Validation of the code with the published study [40] when $\beta et_i = \beta et_e = 0$ and We = 0

| | Rana *et al.* [40] | FEM |
|---|---|---|
| $\mathscr{F}''(0)$ | 0.64479203 | 0.5217220983 |
| $\mathscr{g}''(0)$ | 0.76390721 | 0.17292551291 |

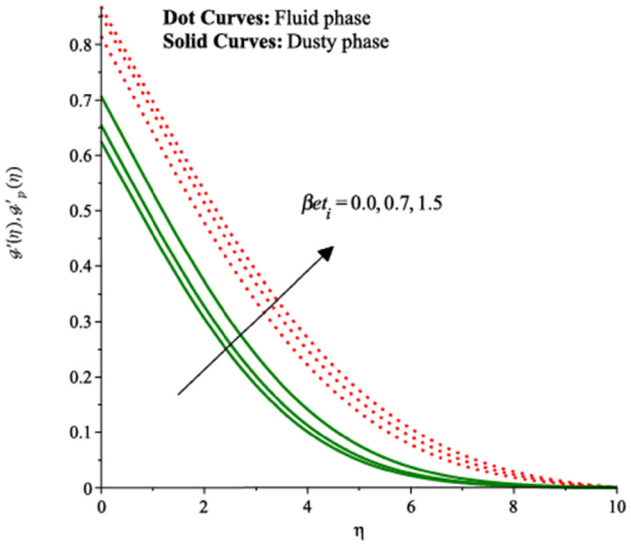


**Figure 2:** Velocity curves (along *x*-axis) under variation in $\beta et_i$.

associated with ternary HNF is resolved by advanced FEM. According to this approach, numerical solutions are

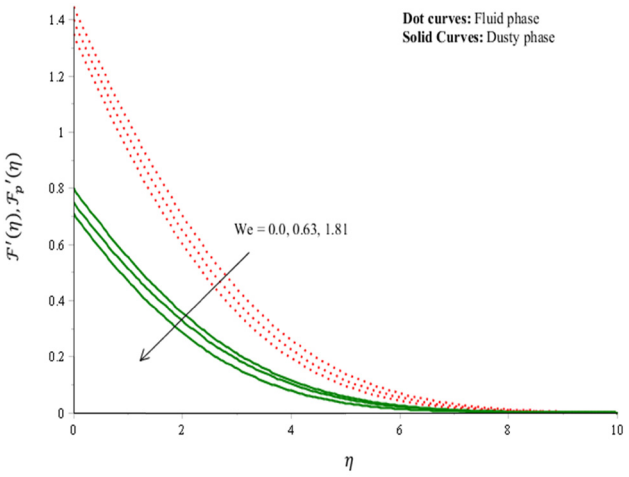


**Figure 4:** Velocity curves (along *x*-axis) under variation in We.

resolved successfully by developed models. The detailed discussion of defined parameters on phase and dusty models is given below.

Figures 2–9 reveal the impacts of We, $\beta et_i$, $\beta et_e$, and $\beta$ on primary and secondary velocity curves for the case of fluid phase and dusty liquid. Here dusty liquid is revealed by solid lines and dot lines reveal the role of fluid liquid. Figures 2 and 6 show the impacts of $\beta et_i$ on primary and secondary velocity curves for fluid phase and dusty liquid. Both velocities (secondary and primary) increase when $\beta et_i$ is enhanced for primary and secondary velocity curves. Ion slip number is a dimensionless number that

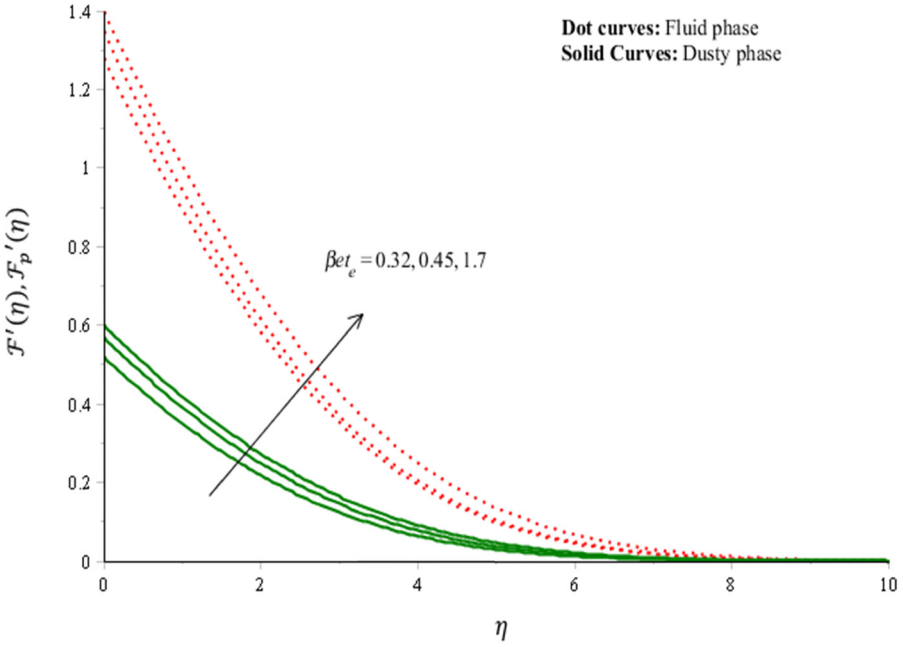


**Figure 3:** Velocity curves (along *x*-axis) under variation in $\beta et_e$.

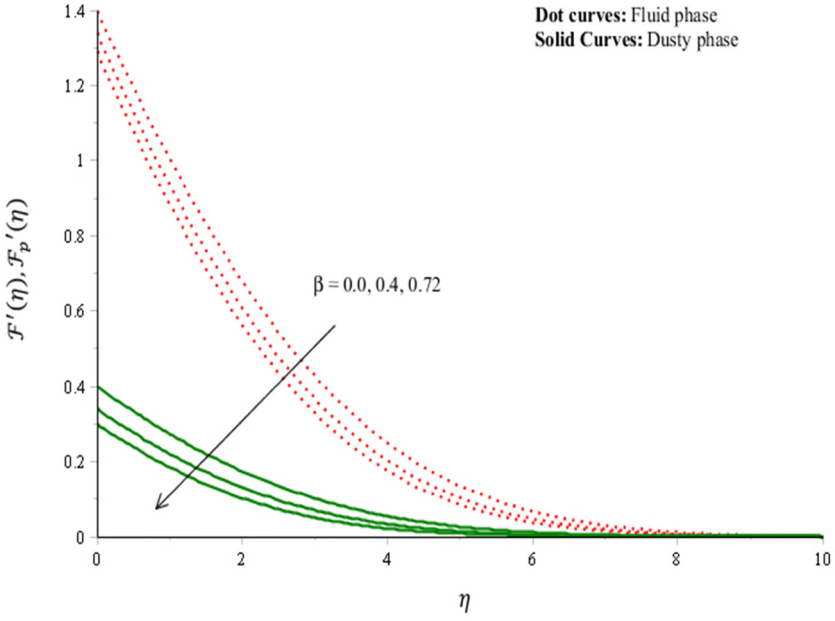


**Figure 5:** Velocity curves (along *x*-axis) under variation in $\beta$.

is applied to knowing neutral particles, and relative velocities. Physically, an enhancement of $\beta et_i$ reveals that the movement of ions is higher than neutral particles. Through collisions, ions can apply momentum to neutral particles. The neutrals accelerate when ions move more quickly and impart more momentum to them. The velocity field as a whole increases as a result of this increased momentum transfer. Figures 3 and 4 illustrate the visualizations of Hall number ($\beta et_e$) on phase velocity and dusty curves. Hall number is utilized for knowing the behavior of Hall impacts that is enhanced due to interactions among electric current and magnetic number, which is carried through charged particles in fluidic motion. It was noticed that the effect of Hall is increased when the Hall number is enhanced. Hall and ion currents are produced when plasma and a magnetic field interact. The force of the magnetic field is opposed by the Hall and ion slip forces created by these currents. As a result, the Lorentz force is produced

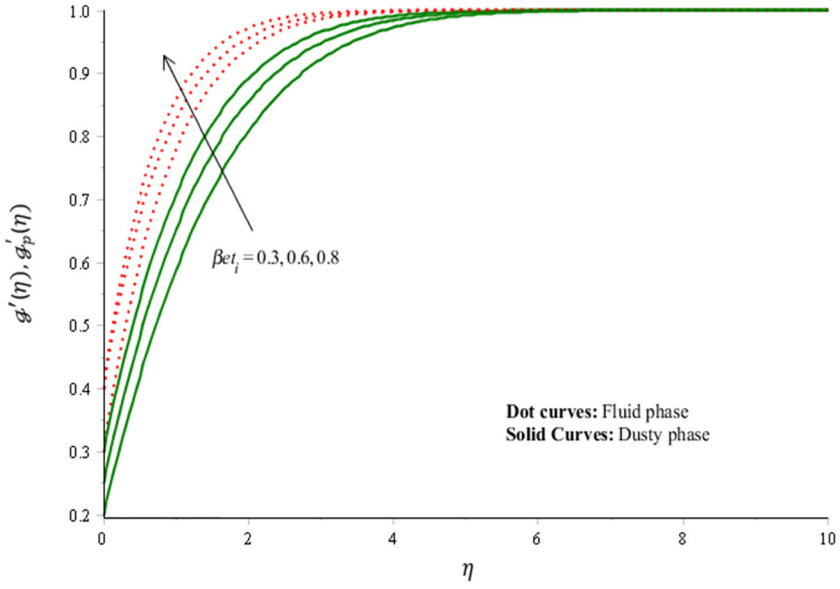


**Figure 6:** Velocity curves (along *y*-axis) under variation in $\beta et_i$.

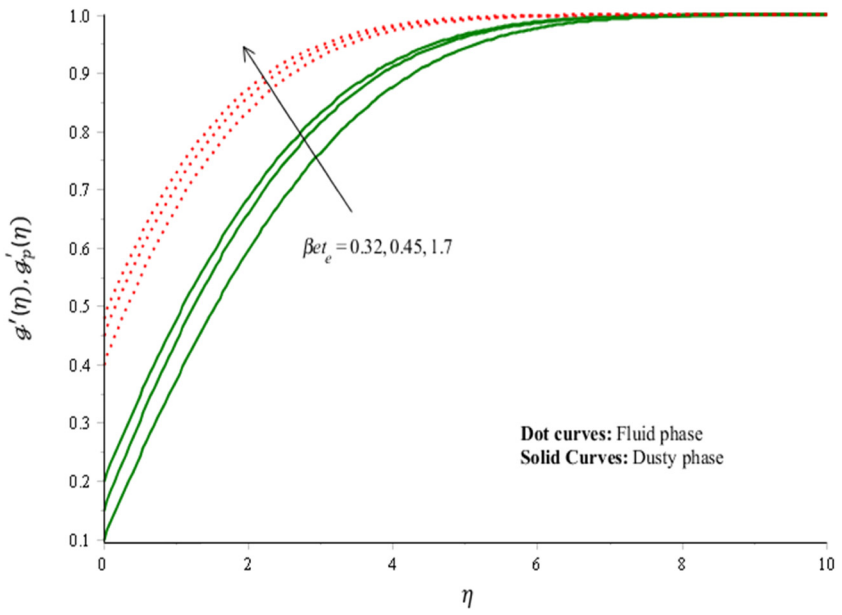


**Figure 7:** Velocity curves (along *y*-axis) under variation in $\beta et_e$.

when the magnetic field is applied to charged particles. The Lorentz force is further reduced by strengthening the opposing forces through an increase in the Hall and ion slip parameters. Because it affects both the general dynamics of magnetic fields and the behavior of charged particles, this effect is especially significant in plasma physics. Therefore, velocity fields are inclined when $\beta et_i$ and $\beta et_e$ are enhanced. Figures 4 and 9 visualize the influence of We on phase velocity and dusty curves. We show the relative contribution of a fluid's elastic and viscous behaviors to flow. Whereas viscous forces are more important when the Weissenberg number is low, a high number suggests that elastic forces predominate. Therefore, frictional force is increased during flow of nanoparticles when We is enhanced. The Weissenberg number is the proportion of elastic force to viscous force. When We = 0, the model becomes Newtonian. The viscous force becomes significant when *We* is enhanced. Due to higher viscous force,

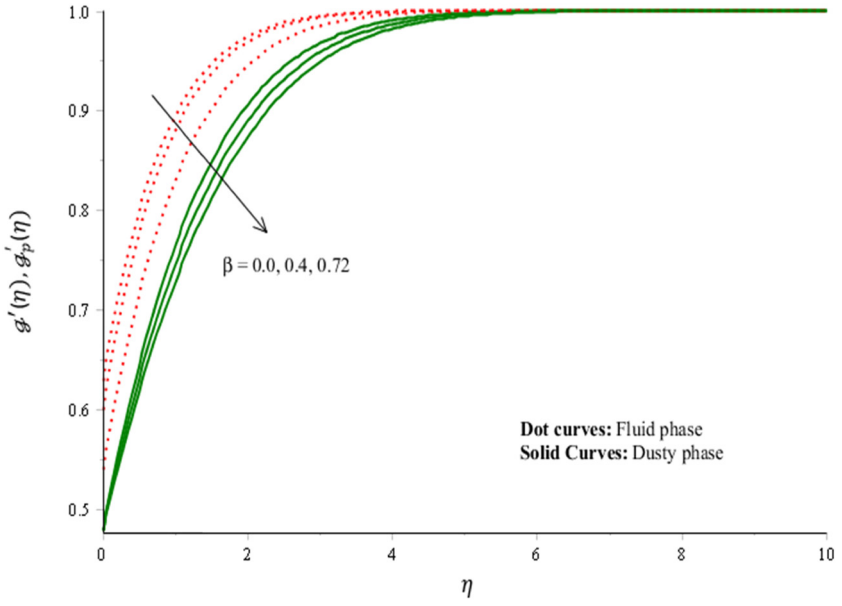


**Figure 8:** Velocity curves (along *y*-axis) under variation in $\beta$.

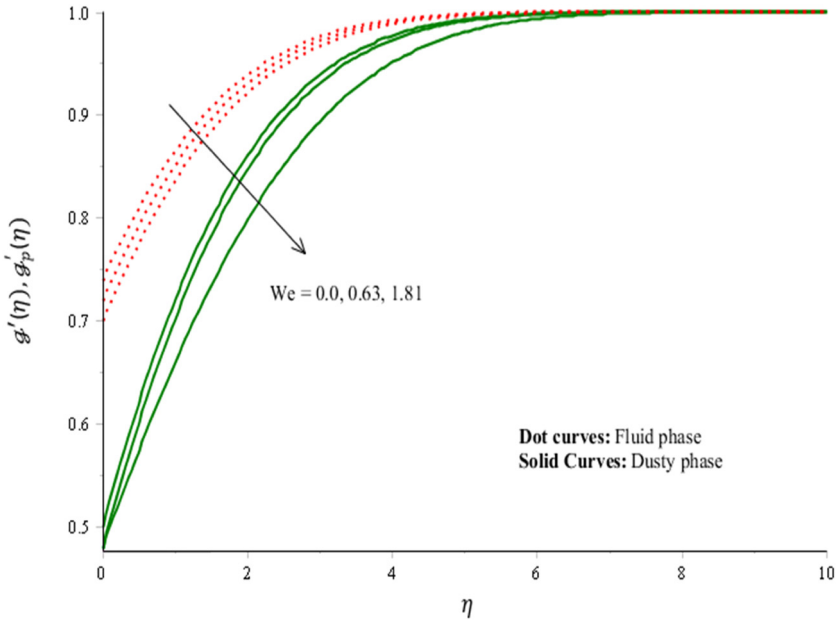


**Figure 9:** Velocity curves (along *y*-axis) under variation in We.

resulting flow field declines. Velocity curves (along the *y*-axis) under variation in $\beta$ are addressed in Figures 5 and 8. Secondary velocities slow down with a change in $\beta$. Here $\beta$ is called the pressure gradient parameter and $\beta$ is evaluated as $\frac{2m}{1+m}$. The pressure gradient parameter ($\beta$) is frequently used to connect specific flow properties, like shear rate to pressure variations along the flow direction. Thus, this parameter $\beta$ can adjust how the pressure gradient affects the flow field. A greater $m$ would result in a higher value of $\beta$, indicating that the pressure gradient's effect becomes more significant. On the other hand, $\beta$ likewise decreases to lessen the impact of the pressure gradient when $m$ is small. Hence, velocity curves decrease when $\beta$ is increased.

The temperature curve under variation in Ec for dusty and phase liquid is illustrated in Figure 10. The dimensionless Ec is used to describe the kinetic energy and enthalpy. It notes that Eckert's number describes the impact of viscous dissipation. An inclination of Ec describes a higher

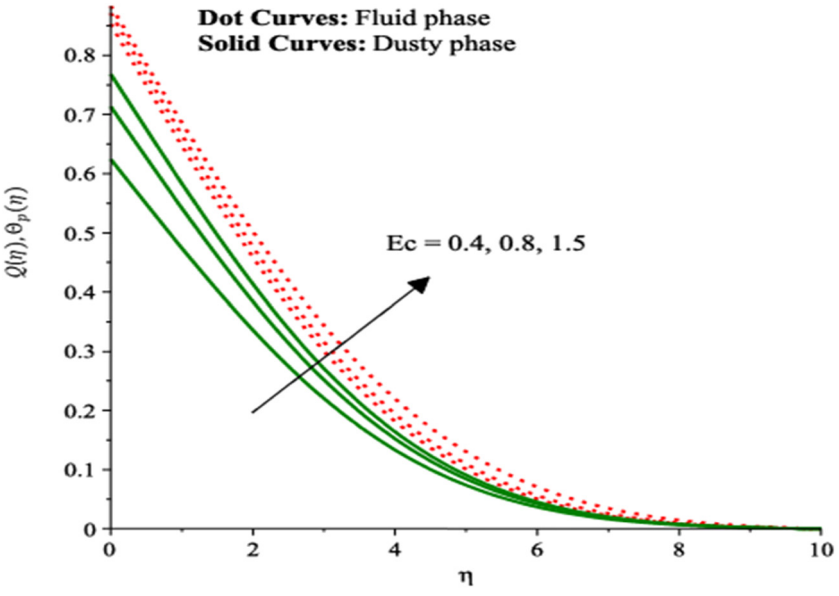


**Figure 10:** Temperature curve under variation in Ec.

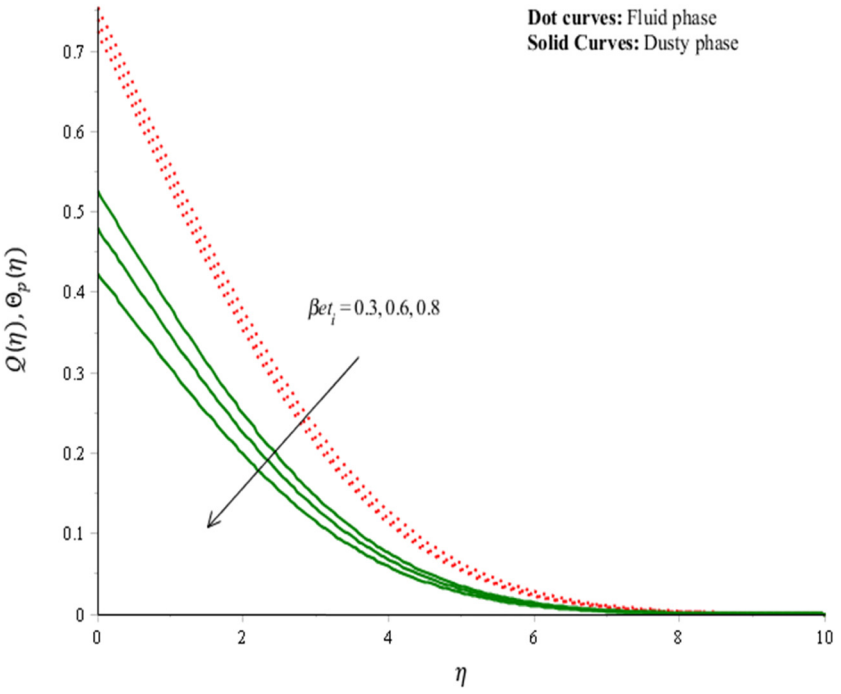


**Figure 11:** Velocity curves under variation in $\beta et_i$.

impact of heat energy. Mathematically, the directly proportional relationship is studied between Eckert number and heat energy. The dimensionless Eckert number illustrates the impact of heat produced by friction in a fluid flow. The impact of this frictional heating increases with an increase in the Eckert number. The fluid's movement produces more heat as the Eckert number increases. The fluid's temperature rises as a result of absorbing this additional heat. The visualization of ion slip number on thermal energy is captured in Figure 11. It is a dimensionless parameter applied to the study of gases that have been ionized, like plasmas. It describes the neutral species and ions moving about one another in the gas. The ion slip number represents the relative velocity between ions and neutrals.

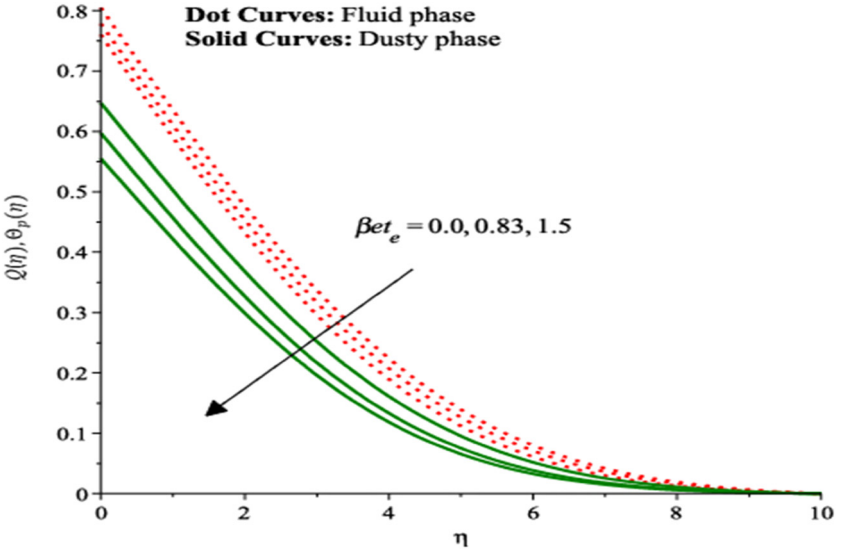


**Figure 12:** Temperature curve under variation in $\beta et_e$.

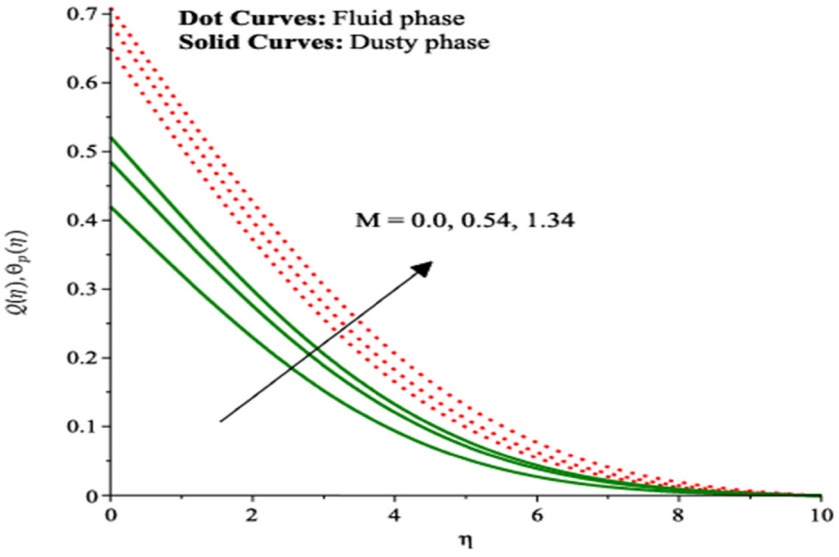


**Figure 13:** Temperature curve under variation in $M$.

It is defined as the ratio of the ion-neutral collision frequency to the ion gyrofrequency. Mathematically, it can be expressed as ($\beta et_i$). It visualizes that $\beta et_i$ has a directly proportional relation with the change in thermal energy. An increase in $\beta et_i$ results in temperature profile enhancement. The temperature curve under variation in $\beta et_e$ is captured in Figure 12 for dusty as well as phase liquids. An increasing role is displayed in thermal energy when $\beta et_e$ is enhanced. It describes the trend of charge carriers subjected to magnetic field. Charge particles experience an electric field and magnetic field (both perpendicular to each other) called the Hall effect. The relationship between the applied magnetic field, current, and induced electric field is quantified by the Hall parameter. Figure 13 shows the effect of the magnetic number on heat energy for dusty as well as phase liquids. Here $M$ occurs using Joule heating.

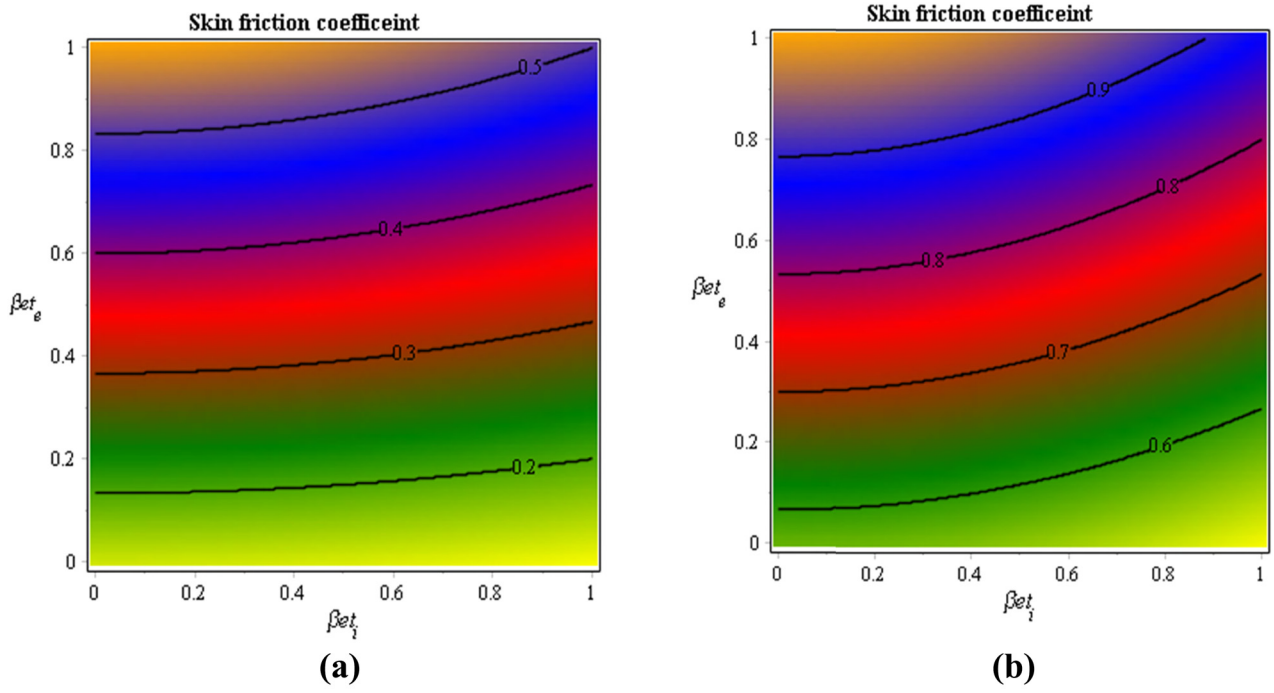


**Figure 14:** Change in divergent velocities under $\beta et_i$ and $\beta et_e$ for phase and dusty fluids. (a) Dusty fluid. (b) Phase fluid.

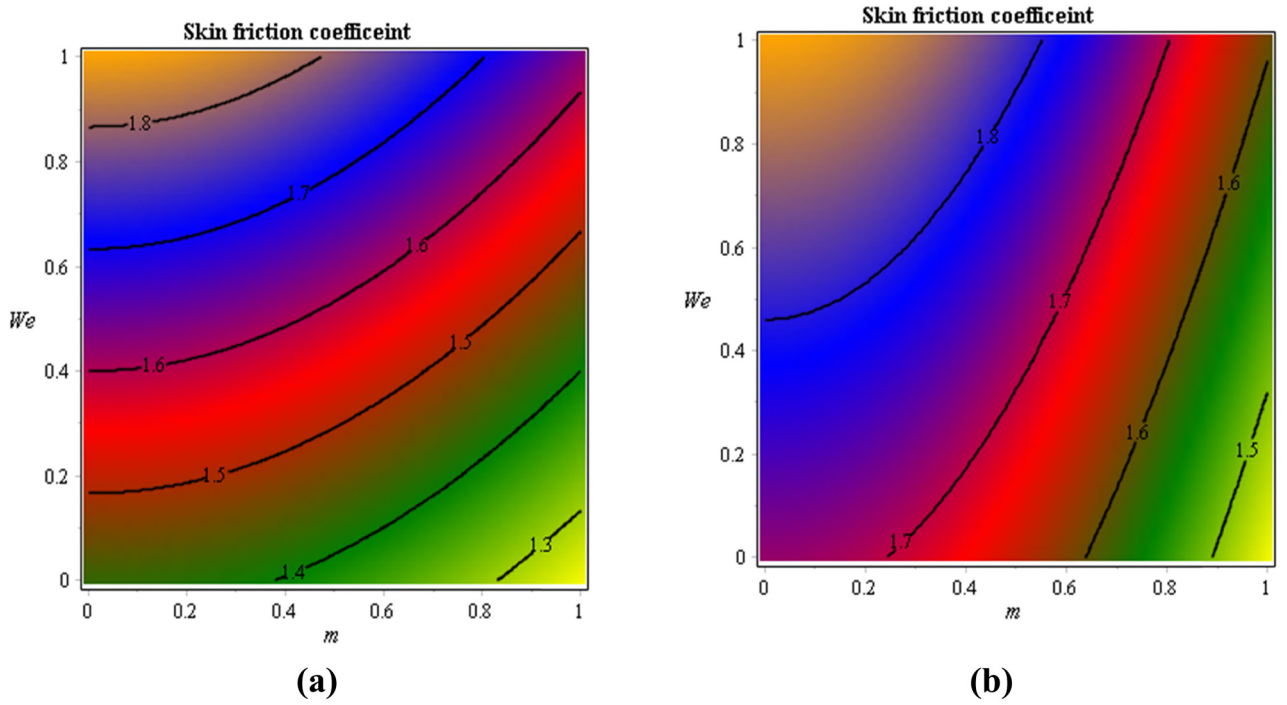


**Figure 15:** Change in divergent velocities under $We$ and $m$ for phase and dusty fluids. (a) Dusty fluid. (b) Phase fluid.

The process by which heat is produced by electric current flowing through a conductor is called Joule heating, or Ohmic heating. Joule's law, which asserts that the square of the current and the conductor's resistance determines the amount of heat produced, explains this phenomenon. The increment in $M$ results in heat energy being enhanced and dissipated significantly. The phenomenon known as Joule heating, or ohmic heating,

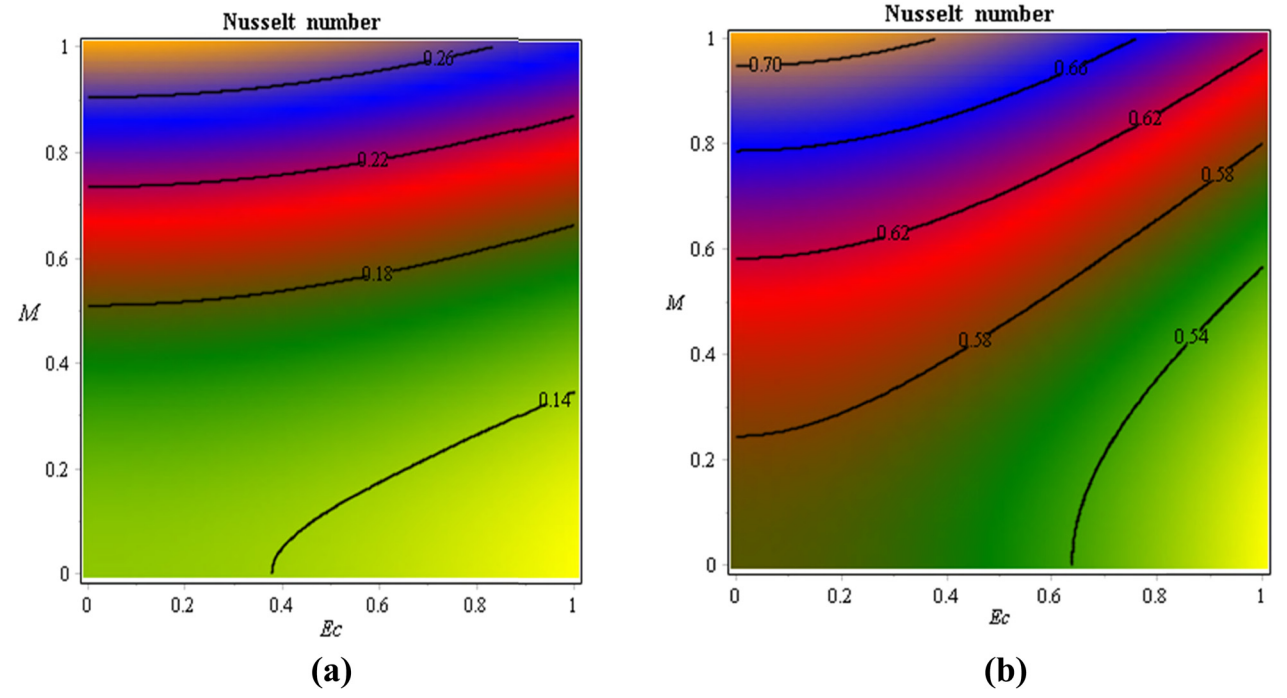


**Figure 16:** Change in temperature gradients under $Ec$ and $M$ for phase and dusty fluids. (a) Dusty fluid. (b) Phase fluid.

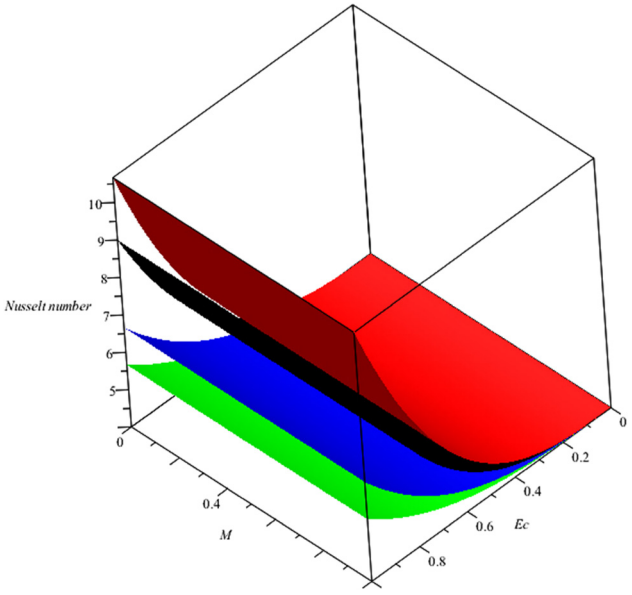


**Figure 17:** Comparative 3D plots of $Ec$ and $M$ on the temperature gradient between tri, hybrid, nanofluid, and working liquid.

**Table 5:** Change in Ec, Pr, $\beta et_i$, $\beta et_e$, and We on temperature gradient for the cases of dusty fluid and phase liquid

| | | Dusty fluid $(\mathrm{Re})^{-\frac{1}{2}}\mathrm{Nu}$ | Phase fluid $(\mathrm{Re})^{-\frac{1}{2}}\mathrm{Nu}$ |
|---|---|---|---|
| | 0.3 | 0.4027932468 | 1.119711288 |
| Ec | 0.4 | 0.3542803692 | 1.081731355 |
| | 0.6 | 0.3111527338 | 1.006274116 |
| | 206 | 0.0613507491 | 1.671369481 |
| Pr | 208 | 0.2297850581 | 1.867330867 |
| | 210 | 0.3798906630 | 1.922025016 |
| | 0.0 | 0.5140671221 | 1.085666460 |
| $\beta et_i$ | 0.3 | 0.6342066683 | 1.188126488 |
| | 0.6 | 0.7416948762 | 1.260256048 |
| | 0.0 | 0.9231750210 | 1.304681068 |
| $\beta et_e$ | 0.8 | 0.948868708 | 1.317159722 |
| | 1.3 | 0.993380714 | 1.338174448 |
| | 0.0 | 0.173224774 | 1.319089034 |
| We | 0.6 | 0.215396722 | 2.324068272 |
| | 1.4 | 0.250209482 | 2.323484074 |

occurs when heat is produced by an electric current flowing through a conductor. This happens because the electrons collide with the atoms and ions in the material as the current passes through the conductor and encounters resistance.

The change in divergent velocities under $\beta et_i$ and $\beta et_e$ for phase and dusty fluids is addressed in Figure 14. The roles of $\beta et_e$ and $\beta et_i$ are used to determine variation in skin friction coefficient (SFC) between dusty and fluidic phases. These characteristics aid in describing the charged particles such as ions and electrons behave when subjected to magnetic and electric fields. SFC is enhanced when $\beta et_i$ and $\beta et_e$ are inclined. Moreover, the phase fluid in SFC is higher than the dusty phase. The change in divergent velocities under We and $m$ for phase and dusty fluids is captured in Figure 15. The characterizations of $m$ and We on SFC between phase fluid and dusty phase are discussed. Because the fluid's elastic energy resists deformation, the decreased elasticity frequently results in a lower skin

**Table 6:** Change in $M$, We, $\beta et_i$, $\beta et_e$, and $m$ on temperature gradient for the cases of $TiO_2/Al_2O_3$/Cu-EG and $Al_2O_3$/Cu-EG

| | | $Al_2O_3$/Cu-EG | | $TiO_2/Al_2O_3$/Cu-EG | |
|---|---|---|---|---|---|
| | | $-(\mathrm{Re})^{-\frac{1}{2}}Cfx$ | $-(\mathrm{Re})^{-\frac{1}{2}}Cfy$ | $-(\mathrm{Re})^{-\frac{1}{2}}Cfx$ | $-(\mathrm{Re})^{-\frac{1}{2}}Cfy$ |
| | 0.3 | 0.6574657074 | 0.7430512048 | 1.7159607396 | 1.7031980705 |
| $M$ | 0.4 | 0.6765520869 | 0.7758504891 | 1.6254364987 | 1.6156856295 |
| | 0.6 | 0.6993437672 | 0.7908548301 | 1.4962478874 | 1.4896434850 |
| | 0.0 | 0.3140376510 | 0.3088790779 | 1.4467961976 | 1.3411062126 |
| We | 0.6 | 0.3397235951 | 0.3355774352 | 1.4657144599 | 1.3612425869 |
| | 1.4 | 0.3778672544 | 0.3540824597 | 1.4803379752 | 1.3966328529 |
| | 0.0 | 0.2786662778 | 0.2751789283 | 1.2452166541 | 1.2420338175 |
| $\beta et_i$ | 0.3 | 0.2516658309 | 0.2484271343 | 1.2204832124 | 1.2775027650 |
| | 0.6 | 0.2265153852 | 0.2234872693 | 1.2753533031 | 1.2926974648 |
| | 0.0 | 0.2029395322 | 0.2000918116 | 1.1545794789 | 1.1520555458 |
| $\beta et_e$ | 0.8 | 0.1807184874 | 0.1780268752 | 1.1348043393 | 1.1323966902 |
| | 1.3 | 0.1996611728 | 0.1372257650 | 1.0978062868 | 1.0955940863 |
| | 0.0 | 0.1205580703 | 0.1182289429 | 1.08254357887 | 1.08040433723 |
| $m$ | 0.8 | 0.1405580703 | 0.1482289429 | 1.08569983234 | 1.09363636840 |
| | 1.3 | 0.1868522531 | 0.1846928404 | 1.09143995103 | 1.14943698119 |

friction coefficient, which can lessen the shear forces applied to the surface. Figure 16 shows the role of Ec and $M$ for phase and dusty fluids on the Nusselt number. Comparative 3D plots of $Ec$ and $M$ on the temperature gradient between tri, hybrid, nanofluid, and working liquid is carried out in Figure 17. The impact of internal friction, or viscous dissipation, on heat transfer is measured by this dimensionless number. Increased heating from fluid particle friction is indicated by higher values of Ec, which raises the temperature gradient. The strength of the applied magnetic field on the fluid is represented by the magnetic parameter. By producing a Lorentz force, increasing $M$ affects the temperature gradient and has the potential to either heat the fluid or change its motion and thermal profile. By increasing the values of $M$ and $E$ results in a decrease in Nusselt number. Table 4 indicates that more heat is retained in the fluid as a result of viscous dissipation when the temperature gradient is reduced by a higher Eckert number. Utilizing both the slip parameter and Hall parameter enhance the temperature gradient in dusty and phase fluids. The temperature gradient rises with higher Pr because thermal diffusion is less efficient. Because elastic effects enhance convective heat transfer, we greatly increase the temperature gradient, particularly in the phase fluid. Table 5 reveals changes in $M$, We, $\beta et_i$, $\beta et_e$, and $m$ on temperature gradient for the cases of $TiO_2/Al_2O_3$/Cu-EG and $Al_2O_3$/Cu-EG. SFC for the case of HNF is less than that for tri-HNF. When $M$ and We are enhanced, SFC is inclined. Because the velocity field decreases when $M$ and We. The gradient close to the surface rises as the velocity falls as a result of this magnetic resistance, increasing SFC. Since the SFC and the rate of velocity change close to the boundary are directly correlated, a stronger magnetic field increases friction at the boundary by lowering fluid velocity. But SFC decreases when $\beta et_i$ and $\beta et_e$ are enhanced. Figure 17 estimates the comparison role of tri, di, and HNF using magnetic number and Ec on Nusselt number. It is experienced that the thermal efficiency of tri-hybrid nanostructures is larger than the thermal efficiency of di and hybrid nanostructures (Table 6).

# 5 Conclusion

The features of HNF in hyperbolic tangent rheology including dusty fluid on a 3D wedge are studied. Hall forces and ion slip currents are considered for visualization of thermal energy. Multiple slip constraints are incorporated with Joule heating. The role of viscous dissipation is also considered. The finite element approach is employed for numerical purposes. The key findings are listed below.

- The study discusses a ternary HNF comprising copper, titanium dioxide, and aluminum oxide suspended in ethylene glycol, highlighting nanomaterial applications in thermal systems. Nanotechnology reviews emphasize research on nanomaterials and their thermal properties, and this study contributes by exploring their behavior under slip conditions, which is essential for real-world applications in cooling, automotive thermal control, and more.
- Thermal efficiency can be maximized by ternary HNFs, a subject of particular interest to industries and researchers working on cooling systems, heat reservoirs, and other related nanotechnology-based thermal applications.
- Utilizing FEM, this approach helps accurate assessment of the behavior of nanofluids in different conditions;
- The motion of the dusty fluid is greater than the motion of phase liquid while momentum boundary layer (MBL) (thickness) for dusty fluid is higher than that for phase liquid;
- The forces (ion slip and Hall effect) bring enhancement thickness (MBL) and motion of fluidic particles;
- With higher values of We, the declination of dusty and phase liquids occurs whereas thickness (MBL) may be managed utilizing change in We;
- Maximum production associated with heat energy may be attained when $Ec$ and magnetic numbers are increased;
- The dusty phase on the temperature curve is greater than the phase liquid on the temperature curve;
- Declination of temperature curves is observed when $\beta et_i$ and $\beta et_e$ are increased;
- Skin friction coefficient are reduced due to the higher values of $m$, We, $\beta et_i$ and $\beta et_e$, while the Nusselt number is increased due to the escalating values of Ec and magnetic field;
- Tri-HNFs' improved heat transfer properties allow them to have a higher thermal efficiency than hybrid and working fluids. This makes tri-HNFs ideal for use in thermal energy and advanced cooling systems;
- The current problem is related to tri-HNF along with Casson fluid. Such development is utilized in solar collectors, enhancing cooling processes, drug delivery systems, drilling muds, oil recovery, viscous food products, electronic devices, cancer treatment, and electronics cooling.

# 6 Future recommendation

The current investigation is constructed on hyperbolic tangent fluid utilizing multiple NF s on the 3D wedge. The

currents (ion slip and Hall effect) are analyzed with dust particles. FEM has been utilized for numerical consequences. In the future, the current model will be analyzed in complex non-Newtonian fluids like Maxwell fluid, second-grade fluid, Bingham plastic, Jeffrey fluid and fourth-grade fluids. Moreover, the current model will be analyzed utilizing advanced correlations of nanofluids like tetra- HNFs and penta-HNFs. FEM will be implemented on PDEs on various complex geometries. Including these effects could result in more thorough models that can be used right away in industrial processes and technologies, increasing the usefulness of your research in real-world and business applications.

**Funding information:** The authors state no funding involved.

**Author contributions:** U.N.: conceptualization, methodology, software, formal analysis, validation; writing – original draft, data curation, and investigation. U.K.: conceptualization, visualization, writing – review and editing, supervision, resources; and writing – original draft. I.M.: validation; writing review and editing; software; writing – original draft, project administration; and funding acquisition. All authors have accepted responsibility for the entire content of this manuscript and approved its submission.

**Conflict of interest:** The authors state no conflict of interest.

**Data availability statement:** The datasets generated and/or analyzed during the current study are available from the corresponding author on reasonable request.

# References

[1] Choi SU, Eastman JA. Enhancing thermal conductivity of fluids with nanoparticles (No. ANL/MSD/CP-84938; CONF-951135-29). Argonne, IL (United States): Argonne National Lab. (ANL); 1995.

[2] Shamshuddin MD, Rajput GR, Mishra SR, Salawu SO. Radiative and exponentially space-based thermal generation effects on an inclined hydromagnetic aqueous nanofluid flow past thermal slippage saturated porous media. Int J Mod Phys B. 2023;37(21):2350202.

[3] Shamshuddin MD, Panda S, Pattnaik PK, Mishra SR. Ferromagnetic and ohmic effects on nanofluid flow via permeability rotative disk: Significant interparticle radial and nanoparticle radius. Phys Scr. 2024;99(5):055206.

[4] Shamshuddin MD, Saeed A, Mishra SR, Katta R, Eid MR. Homotopic simulation of MHD bioconvective flow of water-based hybrid nanofluid over a thermal convective exponential stretching surface. Int J Numer Methods Heat Fluid Flow. 2024;34(1):31–53.

[5] Shamshuddin MD, Saeed A, Asogwa KK, Jamshed W. A semi-analytical approach to investigate the entropy generation in a tangent hyperbolic magnetized hybrid nanofluid flow upon a stretchable rotating disk. J Magn Magn Mater. 2023;574:170664.

[6] Shamshuddin MD, Raizah Z, Akkurt N, Patil VS, Eldin SM. Case study of thermal and solutal aspects on non-Newtonian Prandtl hybrid nanofluid flowing via stretchable sheet: multiple slip solution. Case Stud Therm Eng. 2023;49:103186.

[7] Kumar A, Ray AK, Saha S, Tanwar DV, Kumar B, Sheremet MA. Flow of hybrid nanomaterial over a wedge: Shape factor of nanoparticles impact. Eur Phys J Plus. 2023;138(10):901.

[8] Karthik K, JK M, Kiran S, KV N, Prasannakumara BC, Fehmi G. Impacts of thermophoretic deposition and thermal radiation on heat and mass transfer analysis of ternary nanofluid flow across a wedge. Int J Model Simul. 2024;15:1–13.

[9] Sajid T, Gari AA, Jamshed W, Eid MR, Islam N, Irshad K, et al. Case study of autocatalysis reactions on tetra hybrid binary nanofluid flow via Riga wedge: Biofuel thermal application. Case Stud Therm Eng. 2023;47:103058.

[10] Patil PM, Goudar B, Momoniat E. Magnetized bioconvective micropolar nanofluid flow over a wedge in the presence of oxytactic microorganisms. Case Stud Therm Eng. 2023;49:103284.

[11] Abbasi A, Al-Khaled K, Khan MI, Khan SU, El-Refaey AM, Farooq W, et al. Optimized analysis and enhanced thermal efficiency of modified hybrid nanofluid ($Al_2O_3$, CuO, Cu) with nonlinear thermal radiation and shape features. Case Stud Therm Eng. 2021;28:101425.

[12] Saleem S, Ahmad B, Naseem A, Riaz MB, Abbas T. Mono and hybrid nanofluid analysis over shrinking surface with thermal radiation: A numerical approach. Case Stud Therm Eng. 2024;54:104023.

[13] Sagheer S, Farooq U, Hussain M. Non-similar investigation of enhanced thermal efficiency of Maxwell based hybrid nanofluid (MoS2+ ZnO) across a linearly stretched surface. J Magn Magn Mater. 2023;565:170285.

[14] Sultana N, Shaw S, Mondal S, Nayak MK, Nazari S, Mouldi A, et al. Hall and ion-slip current efficacy on thermal performance of magnetic power-law hybrid nanofluid using modified Fourier's law. Ain Shams Eng J. 2024;15:102838.

[15] Gul H, Ramzan M, Saleel CA, Kadry S. Hall current and ion slip effects on a ternary hybrid nanofluid flow over a bidirectional surface with chemical reaction and Cattaneo–Christov heat flux. Numer Heat Transfer, Part A: Appl. 2023;1–16.

[16] Das S, Barman B. Ramification of Hall and ion-slip currents on electro-osmosis of ionic hybrid nanofluid in a peristaltic microchannel. BioNanoScience. 2022;12(3):957–78.

[17] Krishna MV, Chamkha AJ. Hall and ion slip impacts on unsteady MHD convective flow of Ag-$TiO_2$/WEG hybrid nanofluid in a rotating frame. Curr Nanosci. 2023;19(1):15–32.

[18] Kodi R, Ravuri MR, Veeranna V, Khan MI, Abdullaev S, Tamam N. Hall current and thermal radiation effects of 3D rotating hybrid nanofluid reactive flow via stretched plate with internal heat absorption. Results Phys. 2023;53:106915.

[19] Jameel M, Shah Z, Shafiq A, Rooman M, Vrinceanu N, Alshehri A, et al. Statistical and entropy optimization modeling for radiative hybrid nanofluid flow with Hall effect over exponential stretching/shrinking plate. Int J Thermofluids. 2023;20:100398.

[20] Sharif H, Ali B, Siddique I, Saman I, Jaradat MM, Sallah M. Numerical investigation of dusty tri-hybrid Ellis rotating nanofluid flow and thermal transportation over a stretchable Riga plate. Sci Rep. 2023;13(1):14272.

[21] Khan D, Kumam P, Watthayu W, Jarad F. Exploring the potential of heat transfer and entropy generation of generalized dusty tetra hybrid nanofluid in a microchannel. Chin J Phys. 2024;89:1009–23.
[22] Babu MJ, Sandeep N, Saleem S. Free convective MHD Cattaneo-Christov flow over three different geometries with thermophoresis and Brownian motion. Alex Eng J. 2017;56(4):659–69.
[23] Awais M, Awan SE, Iqbal K, Khan ZA, Raja MA. Hydromagnetic mixed convective flow over a wall with variable thickness and Cattaneo-Christov heat flux model: OHAM analysis. Results Phys. 2018;8:621–7.
[24] Akbar NS, Akram J, Hussain MF, Maraj EN, Muhammad T. Thermal storage study and enhancement of heat transfer through hybrid Jeffrey nanofluid flow in ducts under peristaltic motion with entropy generation. Therm Sci Eng Prog. 2024;49:102463.
[25] Akbar NS, Akram J, Fiaz Hussain M, Maraj EN, Muhammad T. Hybrid nanofluid flow and heat transfer in symmetric porous ducts with CuO nanoparticles and multi-walled carbon nanotubes under peristaltic motion. Mod Phys Lett B. 2024;1–15:2450333.
[26] Adhikari R, Das S, Das S. Neural networks-based framework for recognizing streaming patterns in magnetized Maxwell–Oldroyd-B blood blended with tetra-hybrid nanoparticles and microbes over stenosis in an elastic artery. Eng Appl Artif Intell. 2024;136:109048.
[27] Paul P, Karmakar P, Das S, Das S. Demonstration of angioplasty using a balloon catheter in tetra-hybrid nano-bloodstream within an electrified stenotic arterial cavity under a magnetic field: Artificial neural network analysis. Biomed Signal Process Control. 2024;96:106549.
[28] Lund LA, Asghar A, Rasool G, Yashkun U. Magnetized casson SA-hybrid nanofluid flow over a permeable moving surface with thermal radiation and Joule heating effect. Case Stud Therm Eng. 2023;50:103510.
[29] Lund LA, Omar Z, Khan I. Steady incompressible magnetohydrodynamics Casson boundary layer flow past a permeable vertical and exponentially shrinking sheet: A stability analysis. Heat Transf – Asian Res. 2019;48(8):3538–56.
[30] Asghar A, Dero S, Lund LA, Shah Z, Alshehri MH, Vrinceanu N. Slip effects on magnetized radiatively hybridized ferrofluid flow with acute magnetic force over shrinking/stretching surface. Open Phys. 2024;22(1):20240052.
[31] Yashkun U, Zaimi K, Lund LA. MHD stagnation point flow with thermal radiation and slip effect over a linear stretching sheet. J Mt Area Res. 2023;8:49–59.
[32] Yashkun U, Lund LA, Zaimi K, Shah Z, Alshehri MH, Vrinceanu N, et al. Computational study of magnetite-ethylene glycol–water-based hybrid nanofluid dynamics on an exponential shrinking/stretching Riga surface under radiative heat flux. Colloid Polym Sci. 2024;1–15.
[33] Akbar NS, Rafiq M, Muhammad T, Alghamdi M. Biological structural study for the blood casson fluid flow in catheterized diverging tapered stenosed arteries with emerging shaped nanoparticles: application in drug delivery. Microfluid Nanofluid. 2024;28(6):1–14.
[34] Akbar NS, Rafiq M, Muhammad T, Alghamdi M. Propulsive study of blood flow with heat transfer enhancement connection to ferro copper magnetized nanoparticles in converging tapered stenosed arterial surface. Int J Mod Phys B. 2024;35–47:2550055.
[35] Mekheimer KS, Mohamed El-Sayed MO, Akbar NS, Gouda AA. Physics-informed deep learning study for MHD particle-fluid suspension flow with heat transfer in porous annular-sector duct. Heat Transf. 2024;53(4):1749–69.
[36] Ali A, Das S, Jana RN. Oblique rotational dynamics of chemically reacting tri-hybridized nanofluids over a suddenly moved plate subject to Hall and ion slip currents, Newtonian heating and mass fluxes. J Indian Chem Soc. 2023;100(4):100983.
[37] Sarkar S, Das S. Gyrotactic microbes' movement in a magneto-nano-polymer induced by a stretchable cylindrical surface set in a DF porous medium subject to non-linear radiation and Arrhenius kinetics. Int J Model Simul. 2023;1–18.
[38] Ali A, Das S, Muhammad T. Dynamics of blood conveying copper, gold, and titania nanoparticles through the diverging/converging ciliary micro-vessel: further analysis of ternary-hybrid nanofluid. J Mol Liq. 2023;390:122959.
[39] Ali A, Das S, Jana RN. MHD gyrating stream of non-Newtonian modified hybrid nanofluid past a vertical plate with ramped motion, Newtonian heating and Hall currents. ZAMM-J Appl Math Mech/Z Angew Math Mech. 2023;103(9):e202200080.
[40] Rana P, Gupta S, Gupta G. FEM computations and Taguchi optimization in nonlinear radiative MHD MWCNT-MgO/EG hybrid nanoliquid flow and heat transfer over a 3D wedge surface. Case Stud Therm Eng. 2023;41:102639.
[41] Kudenatti RB, Gogate S SP, Bujurke NM. Asymptotic and numerical solutions of three-dimensional boundary-layer flow past a moving wedge. Math Methods Appl Sci. 2018;41(7):2602–14.
[42] Kudenatti RB, Jyothi B. Computational and asymptotic methods for three-dimensional boundary-layer flow and heat transfer over a wedge. Eng Computers. 2020;36(4):1467–83.
[43] Rana P, Gupta G. Numerical and sensitivity computations of three-dimensional flow and heat transfer of nanoliquid over a wedge using modified Buongiorno model. Comput Math Appl. 2021;101:51–62.
[44] Mohsin BB, Abbas M, Asamoah JKK, Rehman MJU, Umer M, Mahariq I. A computational framework of Marangoni convective flow of trihybrid nanofluid with thermo-bioconvection and oxytactic microorganisms based on the extended version of Xue and Yamada-Ota models. Res Sq. 2024.
[45] Elboughdiri N, Nazir U, Sohail M, Abd Allah AM. Combine thermal performance based on dust particles and Hall and ion slip currents including tetra-hybrid nanoparticles on Howarth's wavy pipe. Results Eng. 2024;23:102666.